PCCP

Accepted Manuscript

ROYAL SOCIETY OF CHEMISTRY

www.rsc.org/pccp

Enhanced removal performance of arsenate and arsenite by magnetic graphene oxide with high iron oxide loading

Fei Yu[a, b], Sainan Sun[a], Jie Ma[b*], Sheng Han[a*]

[a] *School of Chemical and Environmental Engineering, Shanghai Institute of Technology, 100 Hai Quan Road, Shanghai 201418, China*

[b] *State Key Laboratory of Pollution Control and Resource Reuse, School of Environmental Science and Engineering, Tongji University, 1239 Siping Road, Shanghai 200092, China*

**Corresponding author*

Tel.: +86 21 65981831; Fax: +86 21 65981831; E-mail address: jma@tongji.edu.cn (J. Ma)

Tel.: +86 21 60873182; Fax: +86 21 60873182; E-mail: hansheng654321@sina.com (S. Han)

Abstract

Magnetic iron oxide/graphene oxide (MGO) with high iron loading (51 %wt) has been successfully synthesized using the co-precipitation method, and then used as adsorbents for the removal of arsenate and arsenite from aqueous solutions. The resulting MGO possess desirable magnetic properties (12.8 $emu.g^{-1}$) and excellent adsorption properties for the removal of As (III) and As (IV) with significantly enhanced adsorption capacity (54.18, 26.76 $mg \cdot g^{-1}$), which is also much higher than that of other GO-based composites reported previously. The kinetic, equilibrium and environmental effect parameters (pH, ionic strength, coexist anion) were obtained by experimental results. Synchrotron-based X-ray fluorescence microprobe was used to generate elemental distribution maps of adsorbents, the results suggests that the As(V) become preferentially associated with iron oxides during the adsorption process, and the Fe distribution is directly correlated with the As distribution.

Keywords: Graphene; Magnetic; Arsenic; Adsorption; Iron oxide

Introduction

Arsenic is one of the most toxic and carcinogenic chemical elements[1], the presence of arsenic both in natural and anthropogenic sources, which is common due to leaching from minerals or soils, volcanic emission, biological activity, petroleum-refining, industrial waste discharge, mining, and agricultural use of arsenic-containing pesticides, herbicides, fertilizers[2]. Long-term drinking of arsenic-contaminated water can cause cancers of the bladder, lungs, skin, kidney, liver, and prostate[3]. In general, arsenic can exit in both inorganic and organic forms; inorganic arsenic compounds are more toxic than organic arsenic compounds. Most arsenic pollutants in natural water exist as arsenite (As (III)) and arsenate (As (V)) species. Both are toxic, and arsenite is several times more toxic than arsenate. Therefore, it is necessary to synthesis new type adsorbents to simultaneously remove As(III) and As(V) from water with high adsorption capacity.

Up to date, several techniques have been established for arsenic removal, including oxidation/precipitation[4], membrane[5], coagulation/coprecipitation[6], ion exchange methods[7], and adsorption[8]. Among the above methods, adsorption is one of the best available technologies for arsenic removal from drinking water due to its safe and easy operation, high efficiency, regeneration capacity and low cost[9]. So a lot of adsorbents have been used in arsenic removal, such as nano zero-valent iron[10], granular activated carbon media impregnated with zirconium dioxide[11], hydrous titanium dioxide[12], alumina incorporated with copper oxide[13], and magnetic binary oxide particles[14]. Iron hydroxides and oxides (such as amorphous hydrous ferric oxide, ferrihydrite and goethite)[15-18], and iron-based materials are very effective in the removal of arsenic (arsenate and arsenite)[19-21].

Many research showed that reducing the adsorbent size and increasing the specific surface area could improve the removal performance of adsorbent. However, iron oxide nanoparticle adsorbents are easy to aggregate and not easy to separate for small size. So graphene was used as a substrate to loads nanoparticles and avoid agglomeration effectively, magnetic graphene also can be separated use magnet after adsorption, which effectively solves the problem of the nano adsorbent separation.

In this paper, the magnetic graphene oxide (MGO) decorated with iron oxide nanoparticles have been synthesized by a simple co-decomposition method，and then used as adsorbents for removal of arsenate and arsenite from aqueous solutions. The resulting MGO possess desirable magnetic properties and excellent adsorption properties for the removal of As (III) and As (IV) with significantly enhanced adsorption capacity (54.18, 26.76 $mg \cdot g^{-1}$), which is also much higher than that of other GO-based composites reported previously. The kinetic, equilibrium and environmental effect parameters (pH, ionic strength, coexist anion) were obtained by experimental results. Synchrotron-based X-ray fluorescence microprobe was used to generate elemental distribution maps of adsorbents, the results suggests that the As(V) become preferentially associated with iron oxides during the adsorption process, and the Fe distribution is directly correlated with the As distribution.

Experimental method

Materials

All chemicals were purchased from Sinopharm Chemical Reagent Co., Ltd (Shanghai, China) in analytical purity and used in the experiments directly without any further purification. All solutions were prepared using deionized water.

Preparation of graphene oxide

The graphite oxide was prepared using a modified Hummer's method[22-24]. Graphite oxide was dispersed in deionized water and sonicated in an ultrasound bath for 12 h. The sonicated dispersion was centrifuged for 20 min at 4000 r.p.m. to remove unexfoliated graphite oxide particles from the supernatant. The obtained suspension of graphene oxide (GO) was then processed by freeze-drying to obtain GO powder.

Preparation of MGO composite.

1 g graphene oxide was added into 1 L deionized water by ultrasonic dispersion for 13 h. The amount of 0.016 mol of $FeCl_3 \cdot 6H_2O$ was dissolved slowly into the GO solution at room temperature by magnetic stirring and then mixed with intensely stirring for 2.5 h. And excessive ammonia solution was added quickly to precipitate Fe^{3+} ions till

pH up to 10 for 1.5 h. The above solution was heated to concentrate at 100 ℃ before freeze drying process. After freeze drying, the powder was placed into a quartz tube to undergo heat treatment at 723 K and held at this temperature for 2 h under a nitrogen flow, and then the MGO were synthesized.

Characterization methods

The microstructure and morphology of the GO or MGO composites was analyzed by transmission electron microscopy (TEM, JEOL 2100, Japan). X-Ray diffraction (XRD) experiments were conducted on specimens of the magnetic hybrid materials; the X-ray diffractometer (Bruker D8 Advance, Bruker AXS, Germany) was operated at 40 KV and 40 mA. Nickel-filtered Cu_{Ka} radiation was used in the incident beam. Raman spectroscopy (JOBIN-YVON T64000) was used to further characterize MGO. A TA Instruments® Q600 SDT thermal analyzer was used for high-resolution thermogravimetric analysis (TG). TG curves were obtained by heating approximately 10 mg of MGO from 50 to 900°C at a heating rate of 10 °C/min in air. The residual As(V) and As(III) concentrations in solution were determined by an Inductively Coupled Plasma Optical Emission Spectrometry (ICP-OES, Optima 2000, Perkin Elmer, U.K.). Synchrotron-based microprobe experiments were done on Beamline 15U at Shanghai Synchrotron Radiation Facility (SSRF).

Batch sorption experiments

Batch experiments were conducted to evaluate the adsorption performance of As (V) or As(III) on the adsorbents. MGO was selected as adsorbents for As (V) or As (III) adsorption in an aqueous solution. 1000 $mg \cdot L^{-1}$ Stock solution of As (V) and As (III) was prepared by dissolving 4.165 g $Na_2HAsO_4 \cdot 7H_2O$ and 1.73 g $NaAsO_2$, respectively, in 1 L deionized water. And working solutions of required concentrations were obtained by diluting the As (V) and As (III) stock solution with deionized water. All the sorption tests were conducted in well-capped 250 mL flasks containing 50 mL As (V) or As(III) solution with required concentration. After 9 mg of adsorbent was added, the flasks were shaken in a thermostatic shaker at 150 rpm at 298 K for 24 h. All the adsorption experiments were conducted in duplicate, and only the mean values were reported. The maximum deviation for the duplicates was usually less than 5%.

The blank experiments without the addition of MGO were conducted to ensure that the decrease in the concentration was actually due to the adsorption of GO or MGO, rather than by the adsorption on the glass bottle wall. After adsorption, the adsorbent was separated by a 0.45μm membrane. The residual arsenic concentrations in solution were determined by an Inductively Coupled Plasma Optical Emission Spectrometry (ICP-OES, Agilent 720ES, USA). The As(V) and As(III) adsorption isotherm was studied at pH 5, 8，the initial concentration of As(V) or As(III) solution was set from 1 mg/L to 30 mg/L and the adsorption isotherms were then modeled using the Langmuir, Freundlich, and Dubinin-Radushkevich (D-R) isothermal adsorption model.

The amount of adsorbed As(V) or As (III) on adsorbents (q_t , mg/g) was calculated as follows:

$$q_t = (C_0 - C_t) \times \frac{V}{m} \qquad (1)$$

Where c_0 and c_t are the As (V) or As (III) concentrations at the beginning and after a period of time (mg/L); V is the initial solution volume (L); and m is the adsorbent weight (g).

Results and discussion

Characterization of MGO

The image of GO (Fig. 1a, 1b) shows that GO are in the form of flexible sheets. The TEM images of the MGO composites (Fig. 1c,1d) show the presence of iron oxide on GO and crumpled sheets of GO can be seen throughout the morphology. The crumpled silk wave-like graphene sheets and the presence of iron oxide nanoparticles suggest that GO-iron oxide hybrid material is formed. The TEM image (Fig. 1c, 1d) shows that iron oxide nanoparticles are well dispersed on the grapheme surface. The images of MGO show uniform dispersion of spherical iron oxide nanoparticles across the GO matrix. Meanwhile, the average size of the MGO nanoparticles is about ~50 nm.

A representative HRTEM image of iron oxide was shown in Fig.1e, which demonstrated that the attached iron oxide nanoparticles were well crystallized and that the lattice spacing between two adjacent crystal planes was about 0.249 nm; this distance is consistent with the (311) lattice spacing of cubic, Fe_2O_3. The inset in Fig. 1e was the corresponding selected area electron diffraction (SEAD) pattern, obtained from a typical iron oxide nanoparticles confirms the iron oxide to be single crystals. The corresponding selected area electron diffraction (SAED) pattern taken from the graphene/Fe_2O_3 composite, showed diffraction dots belonging to the cubic Fe_2O_3 phase, assigned to the expected crystalline reflections of (311) as shown in Fig. 1e.

The elemental composition of MGO was analyzed by energy-dispersive X-ray spectroscopy (EDS), as shown in Fig. 1f. The EDX results show that the MGO consisted of iron and carbon, and the Cu peaks resulted from the copper grid used to support the MGO.

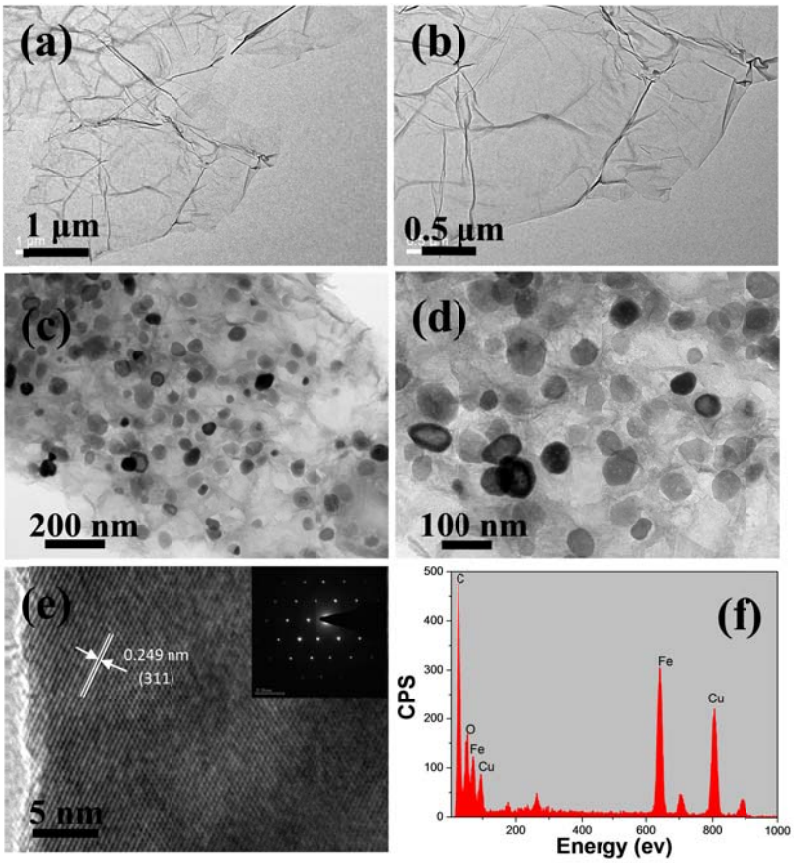

Fig. 1 TEM images of GO (a, b) and MGO (c, d), HRTEM image and SAED (e) of MGO, and EDS spectra (f) of MGO

XRD pattern of the MGO composites were used to elucidate the phase and structural parameters, as shown in Fig. 2a. The d-spacing values of MGO composites were compared with those of standard magnetite (JCPDS card 39-1346) and hematite (JCPDS card 33-0664). The observed diffraction peaks of the composites are in good agreement with those reported in the literature for pure face-centered cubic structured magnetite[25, 26]. The main peaks at 2θ=27°, 24.8°, 35°, 50° show the characteristics of carbon and hematite on the composites, and also the main peaks at 2θ=30°, 42° show the characteristics of magnetite on the composites, besides, the XRD pattern indicates that the surface of the composites contains hematite/magnetite hybrids. So the results confirm that the nanocomposites were composed of carbon，magnetite, and hematite. But as we know Fe_3O_4 has a similar crystal structure to that of γ-Fe_2O_3, it is hard to distinguish between the two on the basis of the XRD pattern alone, and then Raman were selected to analysis the phrase structure of MGO.

Raman spectroscopy is a preferred method to characterize various carbon nanomaterials, metal oxides and biological protein, which is strongly sensitive to the electronic structure. The Raman spectra of GO and MGO are shown in Fig. 2b. The Raman spectra of GO and MGO are characterized by two main features: the D band at about 1329 cm^{-1} arises from a breathing mode of k-point photons of A_{1g} symmetry, the G band at about 1590 cm^{-1} arises from the first order scattering of the E_{2g} photon of sp^2 C atoms. The former is prominent, indicating that GO and MGO contain reduced-size in-plane sp^2 domains due to the extensive oxidation. For MGO, some peaks have been found in the low frequencies (100~800 cm^{-1}), indicating that iron oxide exist in MGO[27]. For MGO, the remaining peak at 210.7 cm^{-1} is assigned to the A_{1g} modes of α-Fe_2O_3, and the peak at 279.7 cm^{-1} is assigned to the T_{2g} modes of Fe_3O_4[28]. The thermogravimetric (TG) analysis of the MGO material is shown in Fig.2c. the TG curves of MGO reveals that in first region it has a little weight loss approach to 5 % below 300 °C, which can be attributed to the evaporation of adsorbed water and the elimination of oxygen-containing functional groups on the surface of MGO. The results shows that MGO contains nearly 51.7 % iron oxide by weight. It is clearly seen that the main thermal events temperature (T_m) decreased from ~400 to

~580 °C, which may be due to the MGO structure defects and more oxygen-containing functional groups. In addition, the DTG curves of MGO exhibit a main peak, and at 538 °C the temperature dropping rate reached the maximum, which shows burning material containing in MGO composites under the temperature does not exist. Besides, along with the increase of temperature, the proportion of material changes also gradually into balance.

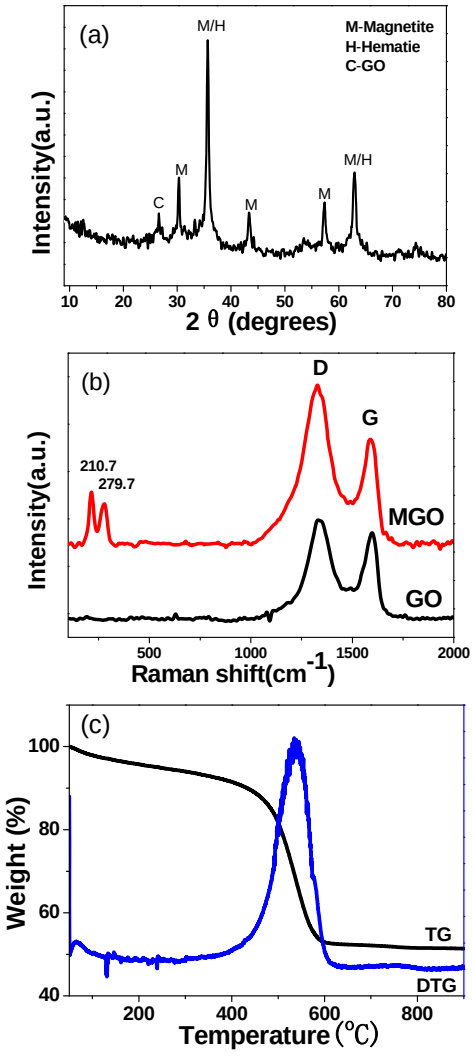

Fig. 2 XRD data (a), Raman spectra (b)，thermal analysis curve (c) of MGO.

The composition of MGO was determined by XPS, as shown in Fig. 3a-d. Fig. 3b is the principal deconvoluted component of the C_{1s} region recorded for the MGO. We can see the strongest peak at 284.3 eV assigned to double bonding carbons for CNTs, which resulted from non-functionalized carbon. The peak at the binding energy

of about 285.0 eV is a consequence of single bonding carbon for graphene[29]. The Fe_{2p} spectrum shows two broad peaks with satellite at 711.4 ev and 724.9 ev representing $Fe_{2p3/2}$ and $Fe_{2p1/2}$ respectively, The $Fe_{2p3/2}$ binding energies for Fe^{2+} and Fe^{3+} were determined by fitting the spectral line shapes to a convolution of Gaussian and Lorentzian functions. The measured $Fe_{2p3/2}$ binding energy is for Fe^{3+}, which compare favorably to the literature values of 710.9-711.2 ev for Fe^{3+30}, and the shake-up satellite line is characteristic of Fe^{3+} in λ-Fe_2O_3. No shake-up satellite line indicated that λ-Fe_2O_3 nanoparticles were not formed on the surface of MGO.

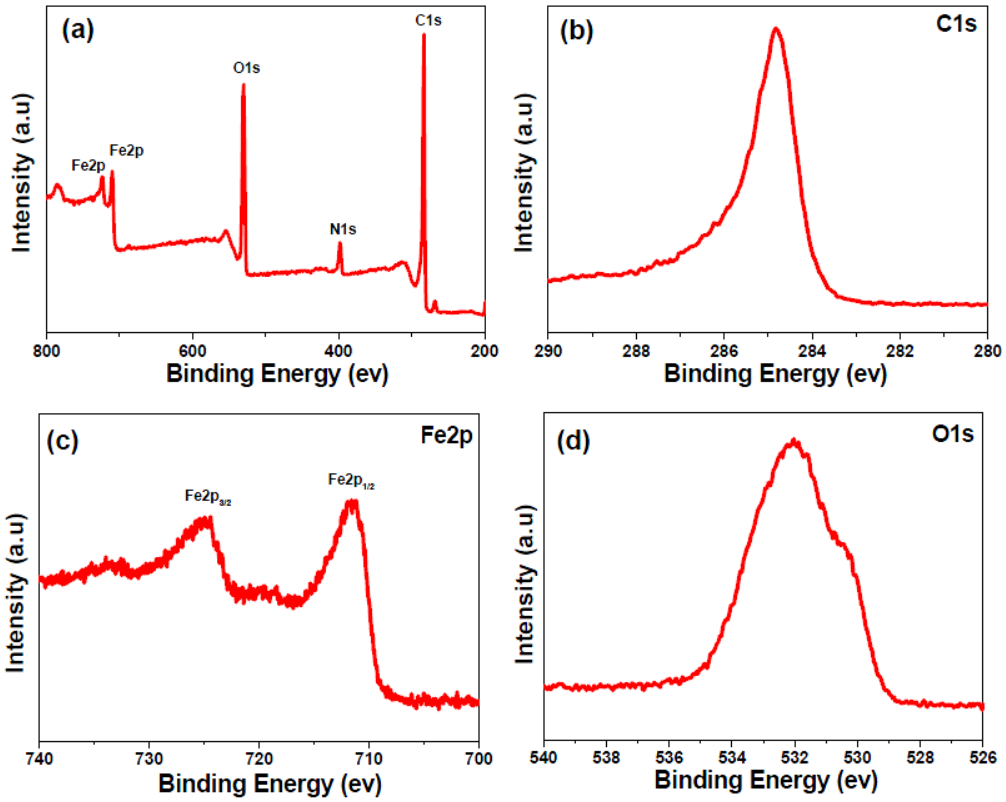

Fig. 3 XPS survey scans of the MGO (a), the C_{1s} region (b), the Fe_{2p} region (c), and the O_{1s} region (d) of MGO.

The N_2 adsorption/desorption isotherms and pore distribution of GO and MGO are presented in Fig. 4. In comparison, the N_2 adsorption/desorption amount of GO is considerably higher than that of MGO at low or high pressure. The detailed features of meso-pore and micro-pore analyzed by the BJH and DFT method are presented in

Table 1. The SSA of MGO drastically decreased by about ~2 times than GO. Such decreases correspond to a decrease in mean pore volume from ~0.713 $cc \cdot g^{-1}$ to ~0.114 $cc \cdot g^{-1}$.

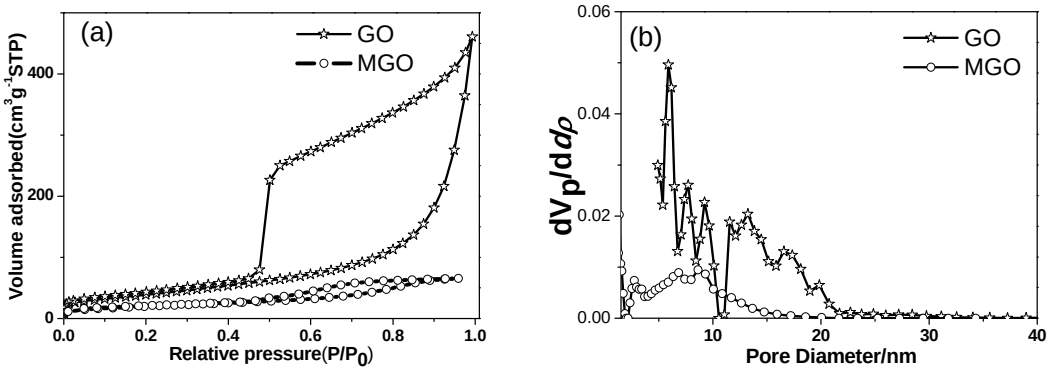

Fig. 4 N_2 adsorption/desorption isotherms (a) and pore size distribution (b) of GO and MGO.

Table 1 Physical properties of GO and MGO.

Samples	SSA	Average pore size	Total pore volume	Micropore	Mesopore
	$m^2 \cdot g^{-1}$	nm	$cc \cdot g^{-1}$	$cc \cdot g^{-1}$	$cc \cdot g^{-1}$
GO	138.20	3.946	0.713	0.056	0.657
MGO	70.20	2.497	0.114	0.011	0.103

The magnetization properties of MGO were investigated at room temperature by measuring magnetization curves (Fig. 5a), the saturation magnetization M_s of MGO is 12.8 $emu.g^{-1}$ (magnetic field=$\pm$20 kOe), indicating that MGO has a higher magnetism. The loop of MGO exhibit very low coercive filed and remanence values, which indicated that MGO are very close to behaving as superaramagnets at room temperature. This simple magnetic separation experiment (Fig. 5b) confirms that MGO can be used as a magnetic adsorbent to remove pollutants from aqueous solutions by using a magnet. The separation is almost completed in 15s. Thus, it illustrated the composites are magnetic and can be effectively removed after the adsorption process.

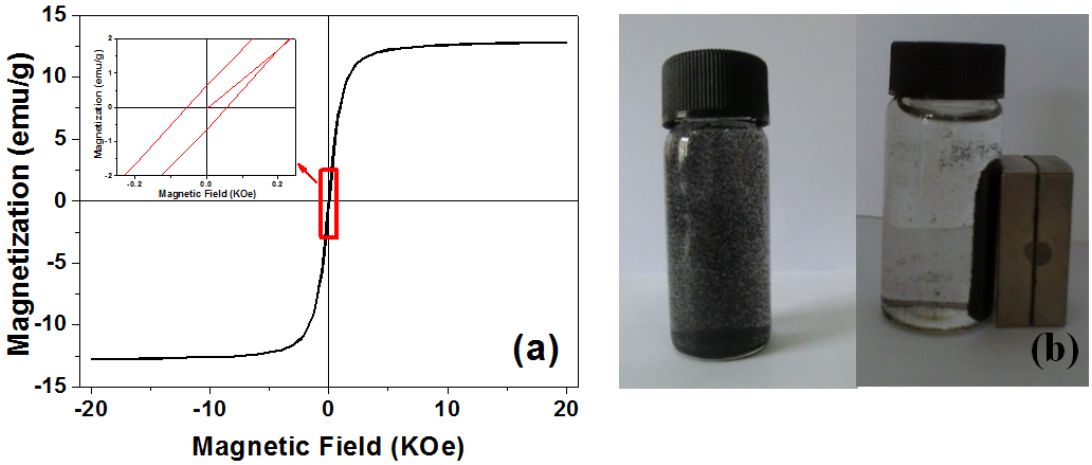

Fig. 5 Room-temperature magnetization curve (a) and magnetic separation photograph (b) of MGO

Adsorption Isotherms

The experimental results of dosage effect for As(III) and As(V) adsorption on MGO, as shown in Fig. 6. It was observed that the adsorption capacity of As(III) and As(V) decreased as the MGO dosage increased over the range 450 to 3000 mg/L. High MGO dosage may increase the viscosity and inhibit the diffusion of As(III) and As(V) to the surface of MGO. Considering the cost, operability, adsorption capacity, and accurate weigh, so adsorbent dosage was selected as 9 mg.

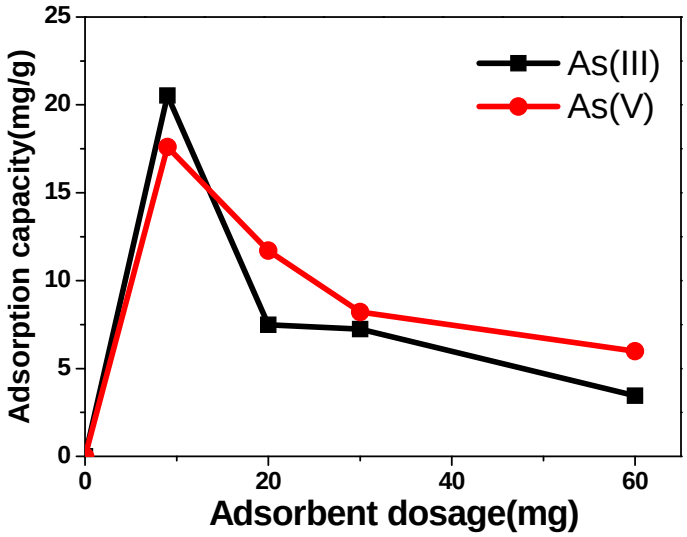

Fig. 6 Effect of adsorbent dosage for As(III) and As(V) adsorption (The pH of As (III), As(V) was 8 and 5, the initial concentration of As (III), As(V) was 8.35 mg/L

and 10.35 mg/L, solution volume: 20ml, contact time: 24 h, agitation speed: 150 r/min)

In this paper, graphene were used as a substrate to load the iron oxide, not as adsorbents. We have test the adsorption performance of GO and MGO, as shown in Fig. S1. The results showed the graphene have little adsorption capacity for arsenate and arsenite, the excellent adsorption properties can be attributed to the iron oxide on the graphene[31, 32]. To evaluate the adsorption capacity of the MGO for As(V) and As(III), the equilibrium data was fitted by Langmuir, Dubinin-Radushkevich and Freundlich models. Fig. 7 shows the isotherms based on the experimental data and the parameters obtained from nonlinear regression using adsorption models are shown in Table 2. By comparison of regression coefficients (R^2) of the three models. It is obvious that Freundlich isotherm model showed a better fit with adsorption data than Langmuir and Dubinin-Radushkevich isotherm model. The Freundlich constant n is found to be greater than 1 which is a favorable condition for adsorption. The maximum adsorption capacity for arsenic ions is shown in Fig. 7 and Table 2. The removal capacity of As(III) is higher than that of As(V) with MGO. The adsorption capacity of MGO is also much higher than that of other GO-based composites reported previously (Table 3).

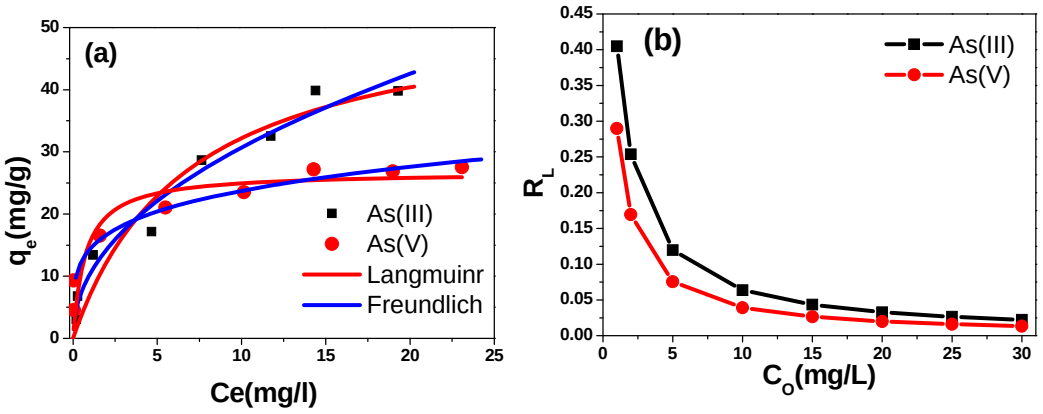

Fig. 7 Equilibrium adsorption isotherms (a) and separation factor R_L(b) of As(III) and As(V) on MGO.

Table 2 Langmuir, Freundlich and Dubinin-Radushkevich isotherms parameters of As (III) and As(V) adsorption on MGO

Adsorbate	Langmuir model			Freundlich model			Dubinin-Radushkevich model			
	K_L(l/mg)	q_m(mg/g)	R^2	K_F	1/n	R^2	B(mol/kJ^2)	Qm(mg/g)	E(kJ/mol)	R^2
As(III)	1.47	54.18	0.908	32.5	0.1	0.988	0.1	28.22	2.236	0.873
As(V)	2.45	26.76	0.837	106.4	0.12	0.996	0.02	23.26	5.0	0.788

Table 3 Comparison of the adsorption capacity of arsenic on MGO with other reported adsorbents

Adsorbent	Solution pH range		Adsorption capacity (mg·g^{-1})		References
	As(Ⅲ)	As(Ⅴ)	As(Ⅲ)	As(Ⅴ)	
MGO	8	5	54.18	26.76	This work
Magnetite-reduced GO	7	7	13.10	5.83	[33]
Fe_3O_4-GO-MnO_2	2-10	2-8	14.04	12.22	[34]
GO/ferric hydroxide	4-7	-	-	23.78	[35]
Magnetic G	7	-	11.34	-	[36]
Manganese-incorporated iron(III) oxide-G	7	-	14.42	-	[37]

The Freundlich constant K_F, is defined as an adsorption or distribution coefficient which describes the amount of arsenic adsorbed on the adsorbents for the unit equilibrium concentration. The K_F values of the MGO were 32.5 and 106.4, respectively, which indicated that MGO showed a higher adsorption capacity for As(V) than As(III). The applicability of Freundlich isotherm suggests that different sites with several adsorption energies are involved, and in some cases[38], the intermolecular interactions occur between arsenic and MGO. Fig. 5b represents the calculated R_L values versus the initial concentration of As (V) and As (III) at 25 ℃. All the R_L values were between 0 and 1, indicating that the adsorption of As (V) and

As (III) on the MGO were favorable at the conditions being studied. However, as the initial concentration increased from 1 to 30 mg/L, R_L values decreased from 0.290 to 0.013 for the adsorption of As (V), and R_L values decreased from 0.405 to 0.022 for the adsorption of As (III). This indicated that adsorption was more favorable at higher concentration.

Adsorption Kinetics

Adsorption is a physicochemical process that involves mass transfer of a solute from liquid phase to the adsorbent surface. The kinetics of arsenic ions removal was determined in order to understand the adsorption behavior of the MGO composites. Fig. 8a shows the adsorption data of arsenic ions by MGO at different time intervals. Besides these, to further analyze the behavior of the arsenic ions adsorption process. The adsorption kinetics was analyzed by using different kinetic models. Pseudo-first-order (PF) and pseudo-second-order (PS) kinetic models are adsorption reaction models, which originate from chemical reaction kinetics, as shown in Fig. S2 and Fig. 8b. The adsorption removal of As(III) and As(V) on MGO was found to be rapid at the initial period (~70 min) and then became slow and stagnate with the increase in contact time (~70 to ~240 min), and nearly reached a plateau after approximately 240 min of the experiment as shown in Fig. 8a. The initial rapid adsorption may be due to the large number of available sites in the initial stage. Along with the increasing the adsorption time, the concentration gradients gradually reduce due to the accumulation of adsorbed anions on the surface sites of MGO, leading to the decrease in the adsorption rate of the later stage[39]. A little more time was required for As(III) to reach equilibrium than As(V), which may be attributed to the multiple adsorption mechanism of MGO for As(III).

The overall adsorption process may be controlled by either one or more steps, including outer diffusion, intra-particle diffusion and adsorption of the adsorbates onto active sites[40]. The last step was considered to be fast and thus cannot be treated as the rate-limiting step in the adsorption process[41]. Consequently, the adsorption rate might be controlled by outer diffusion, inner diffusion or both. In order to better

understand the whole process of adsorption, the PF and PS kinetic models were applied to fit experimental data obtained from batch experiments. The kinetic parameters and the determination coefficients (R^2) were determined by nonlinear regression and are given in Table 4. The R^2 values of the PS kinetic model are much higher than those of PF, the calculated q_e values ($q_{e,cal}$) of PS models are close to the experimental ones ($q_{e,exp}$). Therefore, the PS kinetic model is more appropriate to describe the adsorption behavior of As(III) and As(V) onto MGO. But The R^2 values of the intra-particle diffusion model were 0.815 and 0.251, which indicated intra-particle diffusion is not the main adsorption process. Fig. 8c shows the Weber-Morris model. It was also obtained that the regression of q_t versus $t^{1/2}$ was linear and the plots do not pass through the origin, suggesting that the intra-particle diffusion is not the sole adsorption[42].

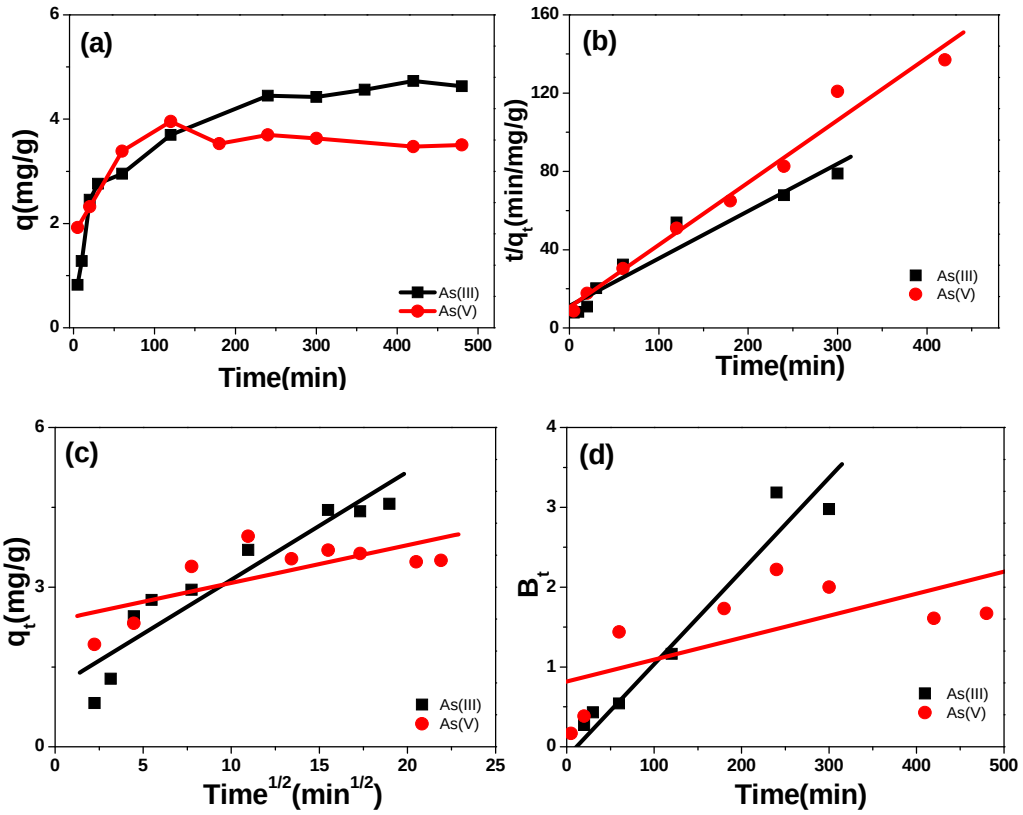

Fig. 8 Kinetic curves (a), pseudo-second-order model (b), Weber-Morris model (c), and Boyd model (d) of MGO.

The adsorption kinetic data was also further analyzed by Boyd model[43]. The

calculated B_t values were plotted against time t as shown in Fig. 8d. The linearity of the plots provides useful information to distinguish between outer diffusion and inner diffusion controlled mechanism of adsorption[44]. In Fig. 8d the plots of adsorption behavior of As(V) do not pass through the origin, confirming the outer diffusion in the entire adsorption process[45], however some plots of adsorption behavior of As(III) pass through the origin, which suggesting intra-particle diffusion and outer diffusion both in the entire adsorption process. These results again confirm the intra-particle diffusion is not the sole adsorption stated in Weber−Morris kinetic model studies.

Table 4 Kinetic parameters of pseudo first- and second-order adsorption kinetic models and intra-particle diffusion model for As (III) and As(V) on MGO. (As (III) concentration=2 mg/L, As(V) concentration=2 mg/L, MGO=0.2 g/L)

Adsorbate	*Initial conc.*	$q_{e,exp}$	Pseudo first-order model			Pseudo second-order model			Intraparticle diffusion model		
	(mg/L)	*(mg/g)*	$k_1(min^{-1})$	$q_{e,cal}$ *(mg/g)*	R^2	$k_2(min^{-1})$	$q_{e,cal}$ *(mg/g)*	R^2	K_i($g•mg^{-1}•min^{-0.5}$)	*C (mg/g)*	R^2
As(III)	2	4.57	0.0073	1.55	0.609	0.013	6.00	0.963	0.186	1.771	0.815
As(V)	2	3.96	0.0037	1.19	0.522	0.007	4.12	0.969	0.038	2.999	0.251

Effect of initial solution pH and final solution pH

The removal of metal ions from an aqueous solution by adsorption is related to the pH values of the solution, as pH affects the surface charge of the adsorbents, the degree of ionization and the different pollutants[46]. Fig. 9 shows the effect of initial pH on the removal of As (III) and As(V) on MGO. It was found that the adsorption of As(V) and As(III) on the adsorbent was evidently dependent on solution pH. Arsenic ion removal on the MGO surface is due to the electrostatic attraction between the positively charged surface of MGO and the negatively charged arsenic/arsenous acid. The pH value dependence of arsenic ions adsorption onto MGO can be explained by point of zero charge (pH_{PZC}) of the adsorbent. At pH lower than pH_{PZC}, the MGO surface is positively charged associated with the protonation of hydroxyl groups on the material surface, whereas at pH lower than pH_{PZC}, negatively charged. As(V) mainly exists as $H_2AsO_4^-$ in the pH range of 3-6, while the divalent anion $HAsO_4^{2-}$

predominates at pH 8-10.5 and AsO_4^{3-} ions become dominant at pH range above 10.5[47]. The As(V) adsorption on MGO below pH_{PZC} 7, which is attributed to electrostatic attraction. The adsorption amount of As (V) increases with increasing pH from 4 to 7, mainly due to the electrostatic attraction between positive surface and $H_2AsO_4^-$ anions. When pH in the 7-11 range, the adsorption amount reaches its maximum and remains unchanged, represents that electrostatic attraction between $HAsO_4^{2-}$, AsO_4^{3-} ions and MGO adsorbent keep a balance. For As (III), as pH value increases, the amount of negatively charged arsenic, which suggests that the electrostatic factors do not sole control the adsorption process onto MGO, surface complexation mainly played an important role in the adsorption process. In Fig. 9, the adsorption amount of As (III) increases with increasing pH from 1 to 4, when pH is in the 4-8 range, the adsorption amount nearly remains unchanged, but when pH above 8, the adsorption amount of As (III) increases, attitudes to surface complexation. The final pH of As (III) and As(V) solution after adsorption was shown in Fig. 9b.

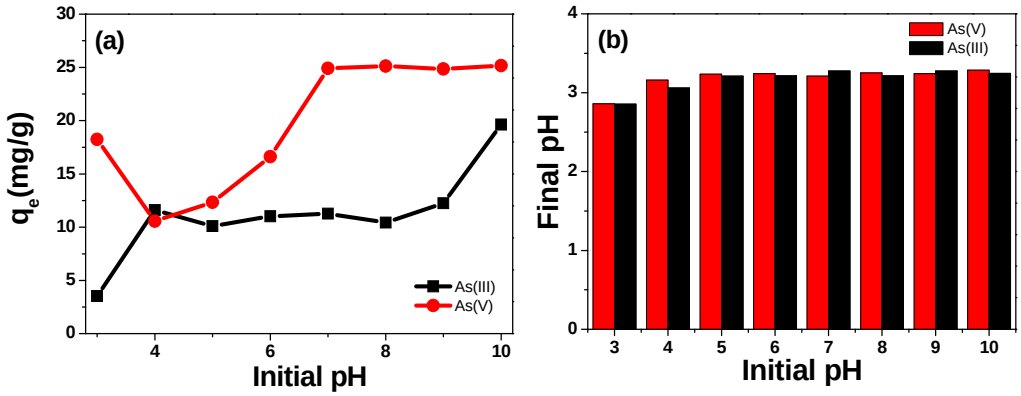

Fig. 9 Effect of initial solution pH and final solution pH on As (III) and As(V) on MGO at 298K and the final pH as a function initial pH. (The initial concentration of As (III), As(V) was 2 mg/L, the dosage of absorbent was 0.2 g/L)

Effect of coexist anion

Sodium chloride as a common chemical agent is often used in our life. So we tested effect of ionic strength on adsorption capacity of As (III) and As (V) on MGO in Fig. S3. For the absorption of As(V), its adsorption capacity increased at the low concentration of NaCl, with concentration of NaCl increasing, the amount of capacity

keep a steady state, but the concentration of NaCl above 4 mmol/L, it showed a trend of decline. This may illustrate high concentration of NaCl effect removing As (V) on MGO. On the other side, the ionic strength on adsorption capacity of As(III) on MGO show the range of concentration of NaCl from 1 to 4.5 mmol/L, as shown in Fig. S3, it slightly reduced adsorption capacity, but with increasing the concentration of NaCl, the adsorption capacity presents a trend of increasing. All these can be ascribed to the competition of sorption sites on the adsorbent between arsenic ion and chloride ion, and the surface complexation.

As well known, various cations and anions may coexist with arsenic ions in natural waters. We investigated NO_3^-, SO_4^{2-}, CO_3^{2-}, SiO_3^{2-}, PO_4^{3-} and F^- anions with arsenic ions in the same environment. Fig. 10 showed the effect of coexist anion on adsorption capacity of As (III) and As (V) on MGO. Under the experimental conditions, NO_3^-, SO_4^{2-}, CO_3^{2-}, SiO_3^{2-} coexisting did not show remarkable influence on As (V) removal by MGO. The F^- anions has shown an evident effect on As (V) removal, due to the competition of F^- with As (V) species for sorption sites. As for As (III), in Fig. 10, it clearly showed SO_4^{2-} and SiO_3^{2-} in the water prevent the complexion between As (III) and surface of MGO, but CO_3^{2-} promoting the adsorption of As (III) by MGO. As expected, PO_4^{3-} caused the greatest decrease in As (V) and As (III) removal efficiency onto MGO. This might be considered that As (V), As (III) and phosphate have the similar tetrahedral structure. Therefore, the great decrease in As (V) and As (III) removal may be related to the competition between them for the adsorption sites. CO_3^{2-} caused the greatest increase in As(III) removal by MGO, which maybe explain CO_3^{2-} with water occurring ionization decomposition, so it occurred OH^- and the promoting pH of the solution, in Fig 9a, it showed the higher pH of As(III) with the high adsorption capacity.

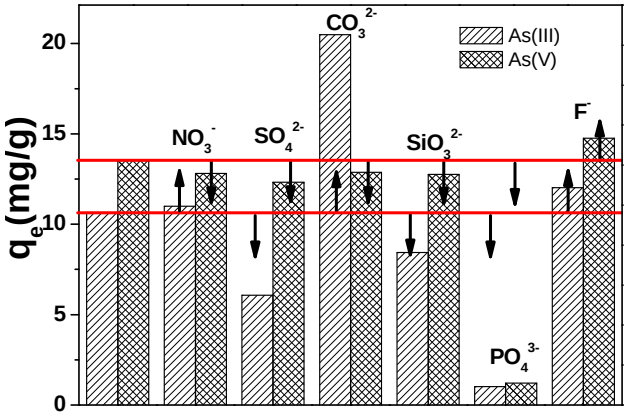

Fig. 10 Effect of coexist anion on adsorption capacity of As (III) and As (V) on MGO. (The initial concentration of As (III), As (V) were all 2 mg/L, the dosage of absorbent was 0.2 g/L. The initial pH of As (III) and As (V) were respectively 8 and 5)

Adsorption-desorption isotherms

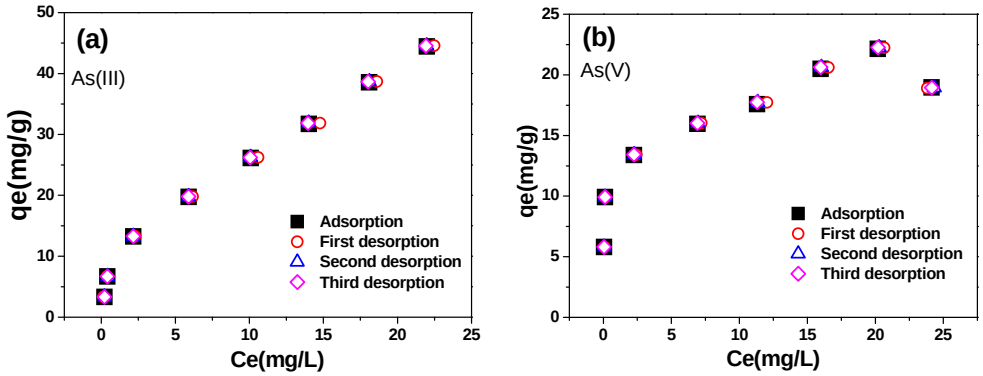

Fig. 11 Adsorption-desorption isotherms of As(Ⅲ) and As (Ⅴ) on MGO.

Fig. 11 shows the adsorption-desorption isotherms of As (Ⅲ) and As (Ⅴ) on MGO. It is evident that all isotherms of MGO had no significant adsorption-desorption hysteresis. Desorption hysteresis may be true or artificial. The latter is caused by an insufficient time allowed for diffusion equilibrium and/or some auxiliary process, which depend on experimental conditions and can be eliminated. At the nearly identical experimental conditions, significant hysteresis of As(Ⅲ) and As (Ⅴ) was not observed for MGO. We think that MGO have the same monomers as the carbon naonotubes. There were no closed interstitial spaces in their aggregates due to their large sheet of paper. As suggested by Yang[48], deformation-rearrangement mechanism

is proposed here because of the monomer geometry and their aggregation behaviour of MGO. Therefore, no adsorption-desorption hysteresis was observed.

Elements distribution analysis

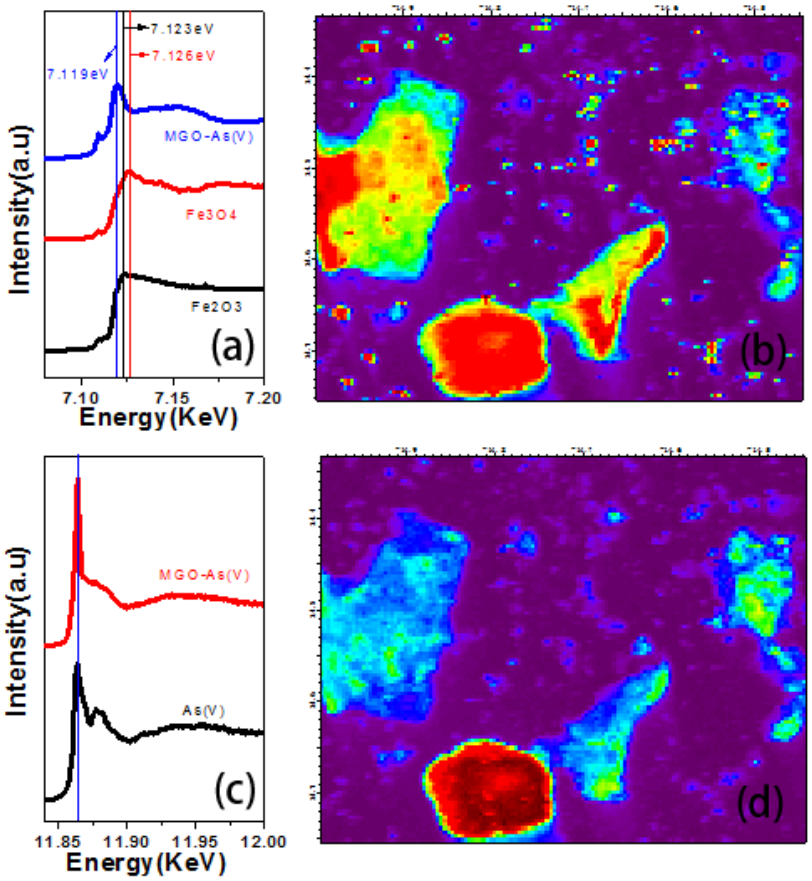

Fig. 12 Normalized As K-edge (a) spectra and element distribution (b), Normalized Fe K-edge(c) spectra and element distribution(d) for MGO-As(IV)

The micro beam X-ray spectroscopy (μ-XAFS) and micro beam imaging experimental research were used to analysis the adsorption mechanism of As(V) on MGO. The elements of sample composition and chemical properties in situ analysis, material structure and the distribution of the two-dimensional were done in line 15U. The position was shown in Fig. S4. MGO XANES signals of before and after the adsorption of arsenic and standards are shown in Fig 12. It clearly observed the MGO-As (V) contained Fe_2O_3 compared with the standard spectra of Fe_3O_4 and Fe_2O_3, which is not corresponded to the XRD pattern and the Raman spectra of MGO composites. The results showed that the Fe (II) were oxidized to the Fe (III) during

the adsorption process of As(V) on MGO. Compared the MGO-As(V) XANES signals with As (V) standards, we can distinctly draw a conclusion that As (V) successfully adsorbed on the surface of MGO, and indicating that the As (V) oxidation state was preserved, could not have caused reduction of As (V) to As (III). The small differences of As (V) XANES spectra before and after adsorption indicated that subtle variations in the electronic surroundings of As (V), are shown in Fig. 11c.

Synchrotron-based X-ray fluorescence microprobe (μ-XRF) was used to generate elemental distribution maps of adsorbents. These results provide direct evidence of the distribution, oxidation states, and speciation of As and Fe in the adsorbents. Using the elemental distribution maps and optical micrographs, distinct aggregates of iron oxide and As (V) were identified, as shown in Fig. 12b and Fig. 12d. This suggests that the As (V) become preferentially associated with iron oxides during the adsorption process, and the Fe distribution is directly correlated with the As distribution. The results also indicated that the little As (V) were adsorbed on the grapheme, which is consisted with the previous reports[49]

Conclusion

To get rid of arsenic ion from aqueous solutions effectively, we developed a new adsorbent magnetic material (MGO) with high iron loading (51 %wt). MGO demonstrates strong magnetization and can be separated by an external magnetic field. The resulting MGO possess excellent adsorption properties for the removal of As(III) and As(V) with significantly enhanced adsorption capacity (54.18, 26.76 $mg \cdot g^{-1}$), which is also much higher than that of other GO-based composites reported previously. It was found that As (III) and As (V) adsorption behavior on MGO can be excellently described by Freundlich model, and the adsorption kinetics was well described by the Pseudo second-order model. More it is worth mentioning, synchrotron-based X-ray fluorescence microprobe was used to generate elemental distribution maps of adsorbents, the results suggests that the As(V) become preferentially associated with iron oxides during the adsorption process, and the Fe distribution is directly correlated with the As distribution. Therefore, MGO is a

promising magnetic nanomaterial for preconcentration and separation of heavy metals for environmental remediation.

Acknowledgement

This research was supported by the National Natural Science Foundation of China (No. 21207100, 51408362), State Key Laboratory of Pollution Control and Resource Reuse Foundation (No. PCRRF14021), "Shu Guang" Project (No. 11SG54), Shanghai Talent Development Funding (No. 201335) and the Shanghai Leading Academic Discipline Project (No. J51503), and Fundamental Research Funds for the Central Universities. We are also thankful to anonymous reviewers for their valuable comments to improve this manuscript.

Reference

1. D. Mohan and C. U. Pittman Jr, Journal of hazardous materials, 2007, 142, 1-53.
2. H. Erdoğan, Ö. Yalçınkaya and A. R. Türker, Desalination, 2011, 280, 391-396.
3. A. Navas-Acien, A. R. Sharrett, E. K. Silbergeld, B. S. Schwartz, K. E. Nachman, T. A. Burke and E. Guallar, American Journal of Epidemiology, 2005, 162, 1037-1049.
4. O. X. Leupin and S. J. Hug, Water research, 2005, 39, 1729-1740.
5. J. Sanchez, A. Bastrzyk, B. L. Rivas, M. Bryjak and N. Kabay, Polym Bull, 2013, 70, 2633-2644.
6. X. Meng, G. P. Korfiatis, C. Christodoulatos and S. Bang, Water research, 2001, 35, 2805-2810.
7. M.-C. Shih, Desalination, 2005, 172, 85-97.
8. C. Y. Han, H. P. Pu, H. Y. Li, L. Deng, S. Huang, S. F. He and Y. M. Luo, J Hazard Mater, 2013, 254, 301-309.
9. S. Saha and P. Sarkar, Journal of hazardous materials, 2012, 227, 68-78.
10. H. Dong, X. Guan and I. Lo, Water research, 2012, 46, 4071-4080.

11. R. Sandoval, A. M. Cooper, K. Aymar, A. Jain and K. Hristovski, Journal of hazardous materials, 2011, 193, 296-303.
12. M. Pirilä, M. Martikainen, K. Ainassaari, T. Kuokkanen and R. L. Keiski, Journal of colloid and interface science, 2011, 353, 257-262.
13. P. Pillewan, S. Mukherjee, T. Roychowdhury, S. Das, A. Bansiwal and S. Rayalu, Journal of hazardous materials, 2011, 186, 367-375.
14. R. M. Dhoble, S. Lunge, A. Bhole and S. Rayalu, Water research, 2011, 45, 4769-4781.
15. S. Fendorf, M. J. Eick, P. Grossl and D. L. Sparks, Environmental science & technology, 1997, 31, 315-320.
16. K. P. Raven, A. Jain and R. H. Loeppert, Environmental science & technology, 1998, 32, 344-349.
17. W. Driehaus, M. Jekel and U. Hildebrandt, J. Water Serv. Res. Technol.-Aqua, 1998, 47, 30-35.
18. C. A. J. Appelo, M. J. J. Van der Weiden, C. Tournassat and L. Charlet, Environmental science & technology, 2002, 36, 3096-3103.
19. V. Chandra, J. Park, Y. Chun, J. W. Lee, I.-C. Hwang and K. S. Kim, Acs Nano, 2010, 4, 3979-3986.
20. S. Shin and J. Jang, Chemical Communications, 2007, 4230-4232.
21. S. Sarkar, L. M. Blaney, A. Gupta, D. Ghosh and A. K. SenGupta, Environmental science & technology, 2008, 42, 4268-4273.
22. W. S. Hummers Jr and R. E. Offeman, Journal of the American Chemical Society, 1958, 80, 1339-1339.
23. M. Hirata, T. Gotou, S. Horiuchi, M. Fujiwara and M. Ohba, Carbon, 2004, 42, 2929-2937.
24. J. Ma, L. Zhou, C. Li, J. H. Yang, T. Meng, H. M. Zhou, M. X. Yang, F. Yu and J. H. Chen, J Power Sources, 2014, 247, 999-1004.
25. X. Li, X. Huang, D. Liu, X. Wang, S. Song, L. Zhou and H. Zhang, The Journal of Physical Chemistry C, 2011, 115, 21567-21573.
26. J. Su, M. Cao, L. Ren and C. Hu, The Journal of Physical Chemistry C, 2011,

115, 14469-14477.

27. J. A. Creighton and R. Withnall, Chem Phys Lett, 2000, 326, 311-313.
28. A. M. Jubb and H. C. Allen, Acs Appl Mater Inter, 2010, 2, 2804-2812.
29. C. C. Chen, C. F. Chen, C. M. Chen and F. T. Chuang, Electrochem Commun, 2007, 9, 159-163.
30. P. C. J. Graat and M. A. J. Somers, Appl Surf Sci, 1996, 100, 36-40.
31. G. S. Zhang, F. D. Liu, H. J. Liu, J. H. Qu and R. P. Liu, Environ Sci Technol, 2014, 48, 10316-10322.
32. S. Vadahanambi, S. H. Lee, W. J. Kim and I. K. Oh, Environ Sci Technol, 2013, 47, 10510-10517.
33. Y. K. Zhang, L. G. Yan, W. Y. Xu, X. Y. Guo, L. M. Cui, L. Gao, Q. Wei and B. Du, J Mol Liq, 2014, 191, 177-182.
34. M. A. Malana, R. B. Qureshi and M. N. Ashiq, Chemical Engineering Journal, 2011, 172, 721-727.
35. K. Zhang, V. Dwivedi, C. Chi and J. Wu, Journal of hazardous materials, 2010, 182, 162-168.
36. J. Zhu, R. Sadu, S. Wei, D. H. Chen, N. Haldolaarachchige, Z. Luo, J. A. Gomes, D. P. Young and Z. Guo, ECS Journal of Solid State Science and Technology, 2012, 1, M1-M5.
37. D. Nandi, K. Gupta, A. K. Ghosh, A. De, S. Banerjee and U. C. Ghosh, Journal of Nanoparticle Research, 2012, 14.
38. B. Chen, Z. Zhu, Y. Guo, Y. Qiu and J. Zhao, Journal of colloid and interface science, 2013, 398, 142-151.
39. J. Hu, D. Shao, C. Chen, G. Sheng, X. Ren and X. Wang, Journal of hazardous materials, 2011, 185, 463-471.
40. S. Rengaraj, Y. Kim, C. K. Joo and J. Yi, Journal of colloid and interface science, 2004, 273, 14-21.
41. F. Yu, J. Chen, L. Chen, J. Huai, W. Gong, Z. Yuan, J. Wang and J. Ma, Journal of colloid and interface science, 2012, 378, 175-183.
42. M. Dogan, H. Abak and M. Alkan, J Hazard Mater, 2009, 164, 172-181.

43. K. V. Kumar, V. Ramamurthi and S. Sivanesan, Journal of colloid and interface science, 2005, 284, 14-21.
44. M. S. Ray, Adsorption Science & Technology, 2000, 18, 439-468.
45. V. Gupta, A. Mittal, V. Gajbe and J. Mittal, Journal of colloid and interface science, 2008, 319, 30-39.
46. D. Iruretagoyena, M. S. P. Shaffer and D. Chadwick, Adsorption, 2014, 20, 321-330.
47. L. Cumbal and A. K. SenGupta, Environmental science & technology, 2005, 39, 6508-6515.
48. Z. Q. Zhao, X. Chen, Q. Yang, J. H. Liu and X. J. Huang, Chem Commun, 2012, 48, 2180-2182.
49. J. Ma, Z. L. Zhu, B. Chen, M. X. Yang, H. M. Zhou, C. Li, F. Yu and J. H. Chen, J Mater Chem A, 2013, 1, 4662-4666.

Graphical Abstract

Magnetic iron oxide/graphene oxide adsorbents with high iron loading were synthesized for the removal of arsenic from aqueous solutions.

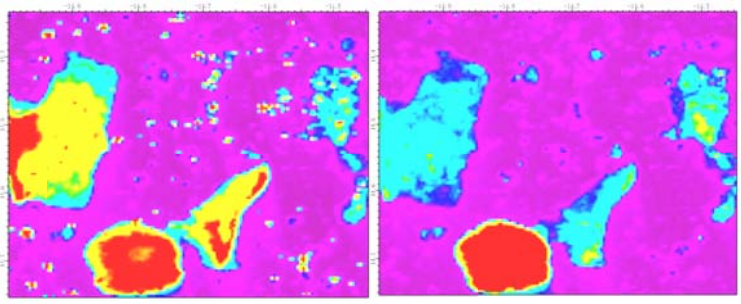

Support information

Data analysis

Isotherm model

Langmuir model

The form of the Langmuir isotherm can be represented by the following equation:

$$q_e = q_m \frac{K_L C}{1 + K_L C} \qquad (1)$$

where q_e is the amount of arsenic adsorbed per gram of adsorbent (mg/g), C denotes the equilibrium concentration of arsenic in solution (mg/L); K_L represents the Langmuir constant (L/mg) that relates to the affinity of binding sites and q_m is a theoretical limit of adsorption capacity when the monolayer surface is fully covered with arsenic molecules to assist in the comparison of adsorption performance (mg/g). Furthermore, the effect of the isotherm shape was studied to understantwhether an adsorption system is favorable or not. Another important parameter, R_L, called the separation factor or equilibrium parameter, which can be used to determine the feasibility of adsorption in a given concentration range over adsorbent, was also evaluated from the relation[23]:

$$R_L = \frac{1}{1 + K_L C_0} \qquad (2)$$

where K_L is the Langmuir adsorption constant (l/mg) and C_0 is the initial arsenic concentration (30mg/l). Ho and McKay[24] established that (1) $0<R_L<1$ for favorable adsorption; (2) $R_L>1$ for unfavorable adsorption; (3) $R_L=1$ for linear adsorption; and (4) $R_L=0$ for irreversible adsorption.

Freundlich model

The Freundlich isotherm model has the following form:

$$q_e = K_F C^{1/n} \qquad (3)$$

where q_e is the amount of arsenic adsorbed per gram of adsorbent (mg/g); C is the equilibrium arsenic concentration in solution (mg/L); K_F and n are the Freundlich

constants, which represent the adsorption capacity and the adsorption strength, respectively. The magnitude of *1/n* quantifies the favorability of adsorption and the degree of heterogeneity of the adsorbent surface.

Dubinin-Radushkevich (D-R) model

The D-R isotherm model has the following form:

$$\ln q_e = \ln q_m - B\varepsilon^2 \qquad (4)$$

B, a constant related to the mean free energy of adsorption (mol^2/kJ^2); q_m, the theoretical saturation capacity; and ε, the Polanyi potential, which is equal to

$$\varepsilon = RT \ln(1 + \frac{1}{C}) \qquad (5)$$

where *R* ($J \cdot mol^{-1} \cdot K^{-1}$) is the gas constant and *T* (K) is the absolute temperature. For D-R isotherm model, from *B* values the mean energy of adsorption. *E* can be calculated using the relation[25]

$$E = \frac{1}{\sqrt{-2B}} \qquad (6)$$

Based on equations (4), (5) and (6), the isotherm constants, *E* and determination coefficients were calculated. The mean energy of adsorption (E) is the free energy change when one mole of the ion is transferred from infinity in the solution to the surface of the solid.

Kinetic model

Pseudo-first and pseudo-second model

The linear form of pseudo first-order rate equation is

$$\ln(q_e - q_t) = \ln q_e - \frac{K_1}{2.303} t \qquad (7)$$

where q_e and q_t are the amounts of MO adsorbed (mg/g) at equilibrium and time *t* (min), respectively; K_1 is the rate constant of the pseudo first-order kinetic model (min^{-1})[24].

A linear form of pseudo second-order kinetic model is express by eq. (8)

$$\frac{t}{q} = \frac{1}{k_2 q_e^{\,2}} + \frac{t}{q_e} \qquad (8)$$

where k_2 is the rate constant($g \cdot mg^{-1} \cdot min^{-1}$) of pseudo second-order kinetic model for adsorption[24].

Weber-Morris kinetics model

Intra-particle mass transfer diffusion model proposed by Weber and Morris can be written as follows[26]:

$$q_t = k_i t^{1/2} + C \qquad (9)$$

where C (mg/g) is the intercept and k_i is the intra-particle diffusion rate constant ($g \cdot mg^{-1} \cdot min^{-0.5}$) for adsorption.

Boyd model

Boyd model [27] has the following form:

$$Bt = -\ln(1 - \frac{q_t}{q_e}) - 0.4977 \qquad (10)$$

where q_t and q_e are the amounts of dyes adsorbed on the adsorbent ($mg \cdot g^{-1}$) at time t (min) and at equilibrium time (minute), respectively; $B = \pi^2 D_i / r^2$ (D_i is the effective diffusion coefficient of the adsorbate and r is the radius of adsorbent particles assumed to be spherical).

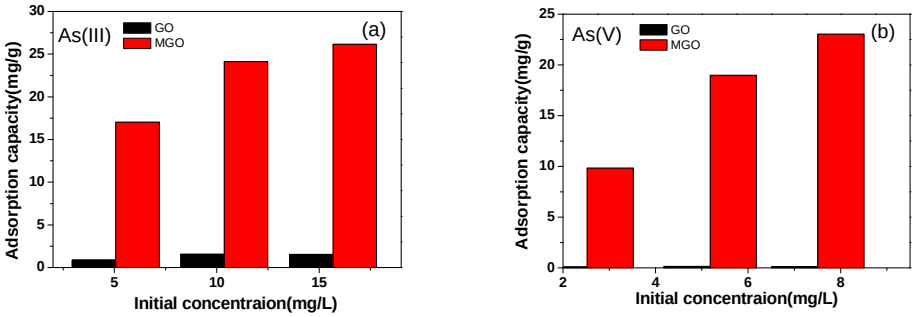

Fig. S1 Comparison of As(III) and As(V) on MGO and GO (The pH of As (III), As(V) was 8 and 5, the dosage of absorbent was 0.25 g/L)

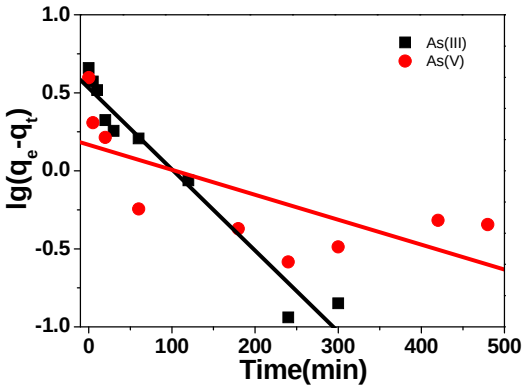

Fig. S2. pseudo-first-order model of As(III) and As(V) adsorption on MGO.

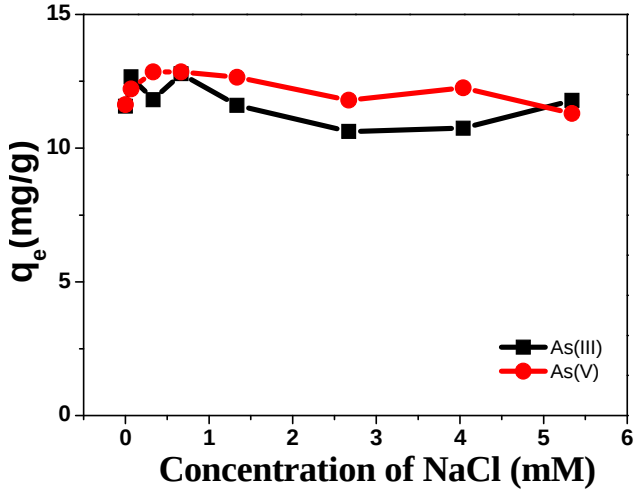

Fig. S3 Effect of ionic strength on adsorption capacity of As(III) and As(V) on MGO.(The initial concentration of As (III), As (V) were 2 mg/L, the dosage of absorbent was 0.2 g/L. The initial pH of As (III) and As (V) were respectively 8 and 5)

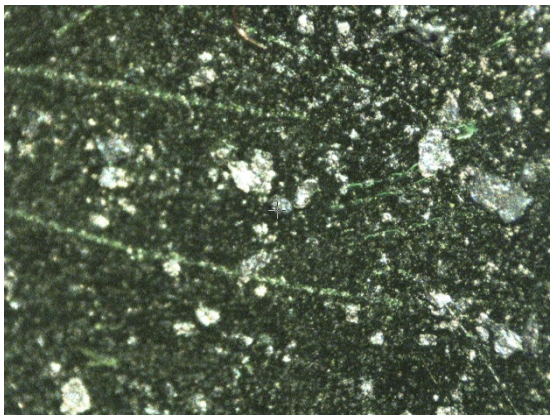

Fig. S4 Photograph of MGO-As(IV)